

# Experimental Time-Modulated Beamformer for Interference Mitigation in a Radio Spectrometer

William C. Barott, *Senior Member, IEEE*, and Sugoon Fucharoen, *Member, IEEE*

**Abstract**—This paper presents experimental results using time modulation to implement inexpensive sidelobe blanking. The Allen Telescope Array is used to save time-series data for the L-band hydroxyl maser W3(OH), which presents a narrow-band source among significant narrow-band interference. A software beamformer processing these data rapidly switches between antenna weights composed of the sum and difference of the acquisition and sidelobe suppression beams. This switching both forms and multiplexes the two beams for the computational cost of a single beamformer, making this technique less expensive than similar approaches. Results show that this approach blanks most sidelobe interference in the experimental data, and also highlight the challenge of coefficient synthesis for sparse arrays.

**Index Terms**—Antenna array, radio astronomy, sidelobe blanking, time modulated array.

## I. INTRODUCTION

**P**HASED array sidelobes are ubiquitous phenomena that present challenges to sensing and communications systems. Ambiguity in the direction of arrival (DOA) of a signal arises when a source is of sufficient strength to be detected in either the main lobe or sidelobes of the beam, and necessitates analysis to resolve the uncertainty. Maisel sidelobe blanking (SLB) [1] is one of many techniques developed to achieve this goal. An SLB detector discriminates main lobe and sidelobe signals (hereafter targets and radio frequency interference, RFI) by comparing the outputs of an acquisition beam (directed toward the target) and a sidelobe suppression (SLS) beam (directed outside the main lobe). While the simplicity of SLB motivates its continued research [2], [3], the need to form two distinct beams can require a computational cost up to twice that of a single beamformer. This cost can be untenable for resource-limited receivers.

Recent work [4] presented a technique for implementing SLB using a time-modulated array (TMA) and digital beamformer, called TMA-SLB. This technique uses a spreading code to multiplex the SLS beam within the acquisition beam during

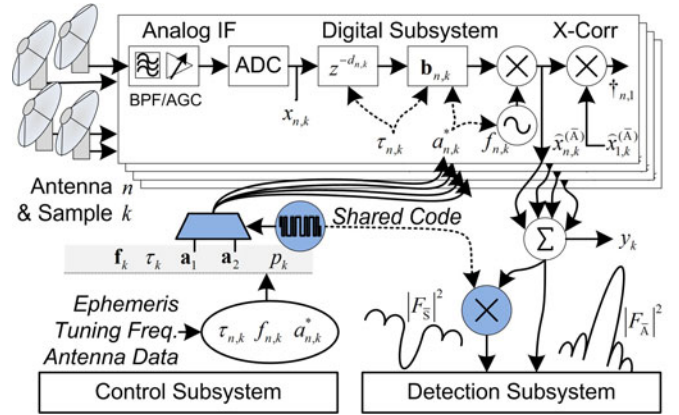


Fig. 1. Overview of the TMA-SLB approach showing that it can be implemented with few additions (blue/dark shaded) to existing systems.

beamforming by rapidly switching the beamformer between sets of antenna weights. This process has an identical computational cost to that of a traditional beamformer, and the SLS beam is recovered using a coherent decoder. As illustrated in Fig. 1, TMA-SLB can be added to an existing beamformer if the weights can be manipulated within sufficient timing constraints.

This paper reports on an experimental study applying TMA-SLB to data recorded at the Allen Telescope Array (ATA), and expands on initial work presented in [5]. A target field was selected to include both a target and significant RFI; these each had bandwidths much less than the system bandwidth, and are hereafter termed narrow-band. Recorded data were processed using a software beamformer that uses TMA-SLB with numerically-optimized weights. Results demonstrate the potential efficacy for the technique as well as challenges of pattern synthesis in large sparse arrays like the ATA.

The paper is organized according to the following outline. First, Section II reviews the current problem, methods of interference mitigation, and TMAs. Section III describes beam multiplexing using a digital TMA, and derives TMA-SLB for both spectrometry and radar applications. Section IV describes the experiment at the ATA, including the array configuration, weight selection, data collection, and analyses. Section V summarizes pragmatic challenges and areas of future work.

## II. BACKGROUND

### A. The Importance of Array Sidelobes

Angular ambiguity enabled by the detection of targets in the sidelobes of antennas and arrays adversely affects both

Manuscript received April 3, 2016; revised August 1, 2016; accepted September 11, 2016. Date of publication October 5, 2016; date of current version February 13, 2017. This work was supported in part by the National Science Foundation under Grant 1547420. The guest editor coordinating the review of this manuscript and approving it for publication was Prof. Wen-Qin Wang.

W. C. Barott is with the Electrical, Computer, Software, and Systems Engineering Department, Embry-Riddle Aeronautical University, Daytona Beach, FL 32114 USA (e-mail: barottw@erau.edu).

S. Fucharoen was with Embry-Riddle Aeronautical University, Daytona Beach, FL 32114 USA. He is now with the Aeronautical Radio of Thailand Company, Ltd., Bangkok 10120, Thailand (e-mail: sfucharoen@gmail.com).

Color versions of one or more of the figures in this paper are available online at <http://ieeexplore.ieee.org>.

Digital Object Identifier 10.1109/JSTSP.2016.2615268

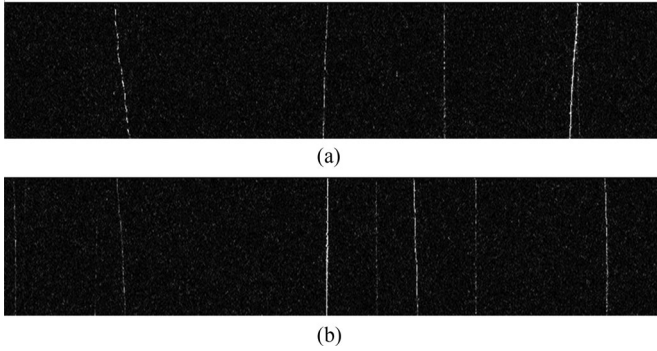


Fig. 2. Typical SonATA waterfalls of intensity versus time (vertical, 93 s) and frequency (horizontal, 533.3 Hz bandwidth at 0.694 Hz resolution). These signals are all presumed to be RFI. Images courtesy of the SETI Institute [14]. (a) 2012-08-09\_20-16-59.UTC.act2.dx1000.id-3.R, 3818.8474 MHz. (b) 2012-08-09\_22-20-39.UTC.act29.dx1000.id-5.R, 3906.5011 MHz.

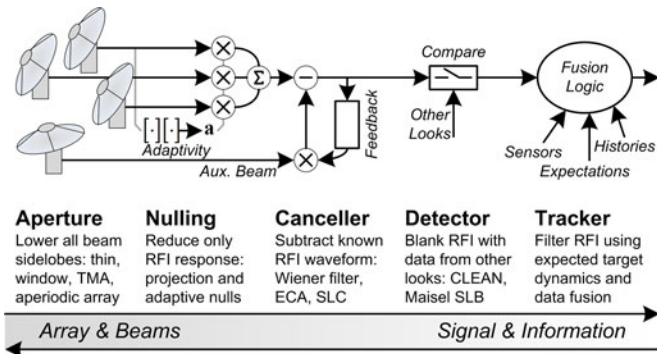


Fig. 3. Approximate relationships and taxonomy of various RFI mitigation techniques.

spectrometers and radars when sidelobe signals are erroneously attributed to the main lobe pointing direction. In scanned-beam or radio imaging systems, sidelobe responses can cause one target to manifest detections at many different pointing angles. Additionally, RFI entering the sidelobes can degrade sensing within the main lobe. Sidelobe mitigation is an important part of common systems, such as aircraft transponders [6]; both common [7] and catastrophic [8] failures related to sidelobe mitigation have been noted.

Sidelobe ambiguities complicate scientific work including retroactive diagnostics of transient phenomena. The strong but brief extragalactic radio burst observed by Lorimer [9] ultimately resulted in the discovery of similar signals [10], but initial follow-up work implicated sidelobe interference for the original detection [11]. Similarly, the 1977 “Wow” signal remains a subject of continuing scrutiny [12], [13] in part because of inconclusive data regarding its DOA. These challenges persist in SETI detectors at the ATA, and Fig. 2 shows that in addition to finding signals, detectors must discriminate legitimate targets from myriad RFI [14].

### B. Methods of Mitigation

A few of the many methods of sidelobe mitigation are arranged by type in Fig. 3. At the highest level, beam design techniques like windowing [15] reduce sidelobes without regard to the interference DOA. Early TMAs [16] emulated windowed

excitations using time-average “on” and “off” antenna states. Large arrays approximate windowing by thinning [17], which evolved from space tapering [18]. Initial interest in sidelobe reduction for irregularly spaced arrays [19] persists in deterministic approaches [20] and optimizers considering both patterns [21] and uv visibilities [22].

For few interferers at known DOAs, pattern nulls [23] can zero the array response of the RFI. This can be difficult in practice, and expected errors between 2.4° and 9° are given for spacecraft DOA predictions by both Früh [24] and Kelso [25]. These errors exceed the beamwidth of systems like the ATA, necessitating adaptive techniques [26], [27]. However, the cost of implementing the correlations required for adaptivity put these techniques out of reach of some large, real-time systems.

RFI not mitigated by the pattern can be cancelled prior to detection using time-domain subtraction. Methods include sidelobe cancellers [28] and related techniques [29], [30] used to remove direct path interference and strong target echoes in passive radars. These techniques incur the associated cost and complexity of an auxiliary beam for each RFI source.

Mitigation in the signal detectors varies by application. Correlator fringe rotation passively suppresses RFI as it passes through sidelobes of alternating phases [31]. Maisel SLB uses knowledge of the patterns of two beams to discard signals detected in the SLS beam [1]. The Högbom CLEAN algorithm [32] extends this concept to image deconvolution, iteratively estimating and removing sidelobe responses of strong sources. Radar ambiguity functions can also be CLEANed to mitigate range and Doppler sidelobes, as shown by Kulpa [33].

Finally, source ambiguities not resolved by other methods can be mitigated by analyzing the detector outputs, often using a tracker. In [34], spatial ambiguity is reconciled by dropping intermittent source tracks attributed to a changing sidelobe structure. Daun [35] proposed likelihood ratio testing for multilateration ambiguity in radar, and noted the possibility of utilizing a priori knowledge of the target’s expected dynamics.

Among these techniques, the characteristics of Maisel SLB are best-suited to the present challenge of mitigating narrow-band sidelobe RFI. As compared to the other methods, SLB requires little a priori knowledge about the RFI type or DOA, and post-processing might reuse existing detectors. Further, beam multiplexing with TMA-SLB reduces the real-time computational costs and enables SLB with existing systems.

### C. Time Modulated Arrays

General sensor arrays combine  $N$  inputs  $x_{n,k}$  at the  $k_{th}$  time sample using weights  $a_{n,k}$  to produce the array output as  $y_k = \sum a_{n,k}^* x_{n,k}$ . Changes to  $a_{n,k}$  over time are often slow and accommodate processes such as tracking, adaptivity, and beam switching. In contrast, TMAs change  $a_{n,k}$  much faster than required for these processes. Analog TMAs usually constrain permissible weights to  $a_{n,k} \in \{0, 1\}$ , implemented with low-cost switches, and design the modulation to emulate more-complex systems or to stimulate behavior only possible with TMAs. Shanks and Bickmore presented the first general discussion of TMAs in 1959 [36]. This was followed by Kummer’s

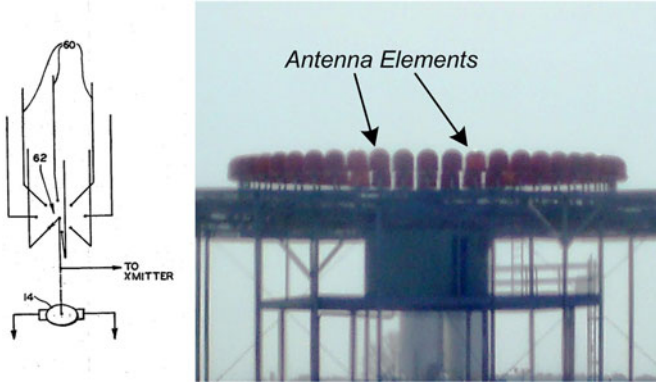


Fig. 4. (Left) Hansel's commutated antennas (from [38]), possibly the earliest TMA. (Right) Photograph of a modern DVOR array.

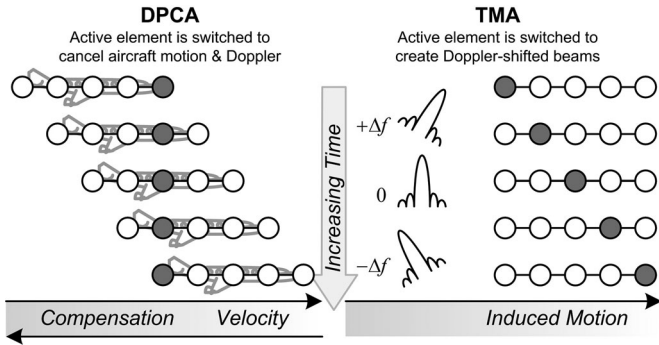


Fig. 5. (Left) The DPCA shifts the array center to cancel aircraft motion. (Right) The TMA moves the phase center to induce Doppler-shifted beams.

investigation of sidelobe reduction [16], and Hatcher's description of TMA harmonic multibeaming [37].

Application-specific TMAs predate Shanks and Bickmore [36] by at least 14 years. Hansel's 1945 patent [38] describes the Doppler VHF Omni Range (DVOR), a radionavigation aid that rapidly switches among radiating elements of an array to cause phase-center motion. This motion results in a direction-dependent Doppler shift emulating the signals of non-Doppler VORs [39]. The DVOR is among the most successful TMAs, composing part of more than 1000 VORs operated by the Federal Aviation Administration (FAA) alone [40]. Fig. 4 shows Hansel's original commutating design [38] along with a photograph illustrating a modern DVOR.

A second early TMA is the displaced phase center array (DPCA), which compensates for Doppler-spread clutter in airborne radars. Shown in Fig. 5, DPCA is credited to Dickey in 1953 [41], but remains a topic of interest in modern radar (e.g., [42]). The linear DPCA aligned with the aircraft's axis cancels the effects of forward motion by successive backward shifts in its phase center. Harmonic multibeam TMAs revisit this technique by using "unidirectional phase center motion" to create Doppler-offset beams [43]. Tong and Tennant [44] describe the TMA timing and array windowing. Lewis and Evins [45] proposed a similar approach to mitigate radar sidelobes, by modulating echoes out of the receiver passband.

The dearth of TMA activity between [37] and the recent resurgence might be attributed to the challenging properties of their patterns. Haupt [46] noted that low-sidelobe TMAs still exhibit strong instantaneous sidelobes and are not as robust to interference as traditional low-sidelobe arrays. Additionally, beam switching can create strong, undesirable sideband radiation at harmonics of the switching frequency. Early work in the present wave of TMA research used optimization algorithms to reduce these harmonic patterns, and includes implementations by Yang [47], Fondevila [48], and Poli [49].

Recent TMAs exhibit behaviors beyond sidelobe reduction, such as adaptive null steering [50]–[53], optimized harmonic multibeaming [54], [55], and direction finding [56]; together, these may support future cognitive radios [57]. Further, Daly [58] used a TMA to apply QPSK in the main lobe of the array and obscure the modulation in the sidelobes. This is similar to TMA-SLB, which applies BPSK only to the sidelobes.

### III. DIGITAL TIME MODULATED ARRAYS AND TMA-SLB

#### A. Multibeaming Approach in TMAs

Classical approaches to TMA multibeaming follow the form given by [16], [37], in which the time-varying array factor  $F(\theta, t)$  is shown to be the sum of discrete harmonic beams as

$$F(\theta, t) = \sum_{m=-\infty}^{\infty} \exp(j2\pi mt/T) \sum_{n=1}^N a_{m,n} \exp(j\frac{2\pi}{\lambda} z_n \cos \theta). \quad (1)$$

The harmonic coefficients  $a_{m,n}$  of  $a_{n,k}$  act as steering weights for the  $n_{\text{th}}$  antenna in the  $m_{\text{th}}$  subbeam of a linear array, here along  $\hat{z}$  with element locations  $z_n$ . Ambiguity among the beams is avoided by using a sufficiently-short TMA period  $T$  so that the separation between harmonics is more than the RF bandwidth of the spectrum of interest, thereby making this approach a frequency-domain beam-multiplexing scheme.

Although most multibeaming TMAs are based on (1), other approaches are possible; each uses unique basis functions to multiplex beams in the array output, at the expense of overall sensitivity. Classical beam switching, for example, represents a time-multiplexed TMA. In [59], the circular DVOR was described as a TMA with single-tone frequency modulation as its basis function. TMA-SLB is derived as a code-multiplexed scheme; it is particularly well-suited for spectrometers having a constrained bandwidth, and that are subject to a set of unknown narrow-band signals exhibiting frequency sparsity.

#### B. Introduction to TMA-SLB

The TMA-SLB approach illustrated in Fig. 1 combines Maisel SLB with TMA multibeaming. This combination is understood by first considering SLB implemented using two separate beamformers. Following the notation of Fig. 1, the outputs  $y_k^{(A)}$  and  $y_k^{(S)}$  represent the  $k_{\text{th}}$  sample of the acquisition and SLS beams, respectively. These are formed using appropriate



weights to sum the antenna samples as

$$\mathbf{y}_k^{(A)} = \sum_{n=1}^N \hat{a}_n^{*(A)} \hat{x}_{n,k}, \quad \mathbf{y}_k^{(S)} = \sum_{n=1}^N \hat{a}_n^{*(S)} \hat{x}_{n,k}, \quad (2)$$

where  $\hat{x}_{n,k}$  is a sample for the  $n_{th}$  of  $N$  antennas and  $\hat{a}_n^{*(A,S)}$  is its weight in each static beam. The arc  $\cdot$  implies that data are calibrated and pre-steered to a desired pointing direction. The matrix form of (2),  $\mathbf{y}_{A,S} = \hat{\mathbf{a}}_{A,S}^H \hat{\mathbf{X}}$ , uses the Hermitian operator  $(\cdot)^H$ . Outputs contain the target  $\mathbf{s}$ , RFI  $\mathbf{r}$ , and noise  $\boldsymbol{\eta}$  as

$$\mathbf{y}_A = \mathbf{s} + g_S \mathbf{r} + \boldsymbol{\eta}_A, \quad \mathbf{y}_S = g_A \mathbf{s} + \mathbf{r} + \boldsymbol{\eta}_S, \quad (3)$$

where  $g_S$  and  $g_A$  represent the gains of each beam in the direction of the other beam. A signal detector  $D(\cdot)$  applied to the beamformer outputs provides a measure of the strength of the detected signals. Basic SLB compares the detector outputs and reports only signals meeting the criteria  $D(\mathbf{y}_A) > D(\mathbf{y}_S)$ .

Signal transport in the receiver is simplified if the beams  $\mathbf{y}_A$  and  $\mathbf{y}_S$  can be effectively multiplexed and later separated. Code division multiple access (CDMA) yields a multiplexed signal  $\mathbf{y}_M$  as  $\mathbf{y}_M = \mathbf{y}_A + W_S \mathbf{p} \circ \mathbf{y}_S$ , where  $\mathbf{p}$  is a code sequence having  $p_k \in \pm 1$ ,  $\circ$  is the Hadamard product in time, and  $W_S$  is a combining weight. The weight  $W_S$  is selected so that  $\boldsymbol{\eta}_M = \boldsymbol{\eta}_A + W_S \mathbf{p} \circ \boldsymbol{\eta}_S$  is similar to  $\boldsymbol{\eta}_A$ , i.e. to minimize the noise added by the combination. When the signals present in  $\mathbf{y}_S$  are sufficiently narrow-band compared to the rate of switching of  $\mathbf{p}$ , they can be suppressed below the resulting noise floor  $\boldsymbol{\eta}_M$ , precluding their detection by  $D$  so that  $D(\mathbf{y}_M) \approx D(\mathbf{y}_A)$ . Similarly, the decoded beam  $\mathbf{p} \circ \mathbf{y}_M = \mathbf{p} \circ \mathbf{y}_A + W_S \mathbf{y}_S$  provides a signal detector output as  $D(\mathbf{p} \circ \mathbf{y}_M) \approx D(W_S \mathbf{y}_S + \mathbf{p} \circ \boldsymbol{\eta}_A)$ . These approximations provide the definitions of the time-average equivalent acquisition and SLS beams as

$$\mathbf{y}_{\bar{A}} = \mathbf{y}_M = \mathbf{y}_A + W_S \mathbf{p} \circ \mathbf{y}_S, \quad (4)$$

$$\mathbf{y}_S = \mathbf{p} \circ \mathbf{y}_M = \mathbf{p} \circ \mathbf{y}_A + W_S \mathbf{y}_S. \quad (5)$$

It is possible to obtain (4) using a single beamformer to both form and multiplex the beams. Merging (4) with (2) gives

$$\mathbf{y}_k^{(\bar{A})} = \sum_{n=1}^N \hat{a}_n^{*(A)} \hat{x}_{n,k} + W_S p_k \sum_{n=1}^N \hat{a}_n^{*(S)} \hat{x}_{n,k}, \quad (6)$$

in which terms can be gathered within one summation as

$$\mathbf{y}_k^{(\bar{A})} = \sum_{n=1}^N \left( \hat{a}_n^{*(A)} + W_S p_k \hat{a}_n^{*(S)} \right) \hat{x}_{n,k}. \quad (7)$$

Grouping  $\hat{a}_n^{*(A)} + W_S p_k \hat{a}_n^{*(S)}$  into a single set of weights gives

$$\mathbf{y}_k^{(\bar{A})} = \sum_{n=1}^N \hat{a}_{n,k}^* \hat{x}_{n,k} \equiv \sum_{n=1}^N \hat{x}_{n,k}^{(\bar{A})}. \quad (8)$$

Time-variations in  $\hat{a}_{n,k}^*$  enable the modulation  $p_k$ . Forming  $\mathbf{y}_{\bar{A}}$  using a TMA removes the typical SLB requirement of a second beamformer, thus reducing the beamforming cost of SLB by half. Each of the steps of SLB detection and blanking are implemented using  $\mathbf{y}_{\bar{A}}$  and  $\mathbf{y}_S = \mathbf{p} \circ \mathbf{y}_{\bar{A}}$ .

TMA-SLB and the following sections use this approach as-written, but a generalization of (7) is possible to consider cases of multiplexing more than two beams. In this case,

$$\mathbf{y}_k^{(\bar{A})} = \sum_{n=1}^N \left( \sum_{m=1}^M W^{(m)} p_k^{(m)} \hat{a}_n^{*(m)} \right) \hat{x}_{n,k}, \quad (9)$$

where  $m$  represents the modulated subbeam number out of  $M$  total subbeams. In general,  $\hat{a}_{n,k}^*$  take on  $2^{M-1}$  unique states to satisfy all combinations of unique sequences  $p_k^{(m)} \in \pm 1$ , although specifically-designed sequences might have as few as  $M$  different states.

TMA-SLB uses  $M = 2$  and has 2 states,  $\hat{a}_1 = \hat{a}_A + W_S \hat{a}_S$  and  $\hat{a}_2 = \hat{a}_A - W_S \hat{a}_S$ , representing two instantaneous beam patterns,  $F_b$ , where  $b \in \{1, 2\}$ . These patterns should relate as  $F_1 = F_2$  within the main lobe and  $F_1 = -F_2$  within the side-lobes. These conditions modulate signals originating in the side-lobe direction without affecting signals originating within the main lobe. However, following (3), the performance of the technique is limited by the achievable responses  $g_S$  and  $g_A$ .

### C. Implementation for Radar

Although TMA-SLB was developed for spectrometry, code-division multibeaming is also suitable for radar applications. Like spectrometers, radars often receive a small number of discrete signals at unknown (but sparse) frequencies, as in Fig. 2. Further, traditional harmonic multibeaming TMAs can be impeded by limitations of the pulse repetition frequency (PRF) imposed by both range and velocity ambiguities.

Radar-based TMAs usually focus on reducing time-average sidelobes rather than multibeaming. Lewis and Evins [45] imposed a rapid TMA sequence onto each transmitted pulse, forcing harmonic responses to correspond to unrealistic target velocities. Li [60] expanded this approach to also modulate received pulses. In contrast, Euzière [61] used a TMA period equal to the radar's coherent processing interval (CPI), but with a slow switching rate not inherently coupled to the PRF. The possibility of target ambiguities arising from sidelobe modulation was not considered; instead, the modulation was considered for opportunistic use for communications [62].

Radars using TMA-SLB can encode sidelobe responses within the cross ambiguity function (CAF). Here, the rate of  $p_k$  must be fast compared to the CPI, rather than the RF waveform. Further, locking the modulation rate of  $p_k$  to the PRF reduces the detector complexity by allowing coherent decoding after formation of the CAF. This alleviates the PRF constraints found in frequency-division TMA multibeaming.

The CAF of a coherent radar is given by cross-correlating a surveillance signal  $\mathbf{y}$  with a matched filter  $\mathbf{c}$  (here, identical to the radar illumination) as  $\boldsymbol{\chi} = \mathbf{c} \star \mathbf{y}$ . This is described as a function of the fast-time delay  $\tau$  and Doppler shift  $f_D$  as

$$\chi_{\tau, f_D} = \sum_{k=k_0}^{k_0 + f_s CPI} \hat{c}_{k-f_s \tau}^* y_k \exp(-j2\pi f_D k / f_s), \quad (10)$$

where  $f_s$  is the sample rate of the RF waveform. The radar can compute the CAF on the beam output [63], [64], but can

also beamform the results of CAFs computed for individual antennas as  $\chi = \mathbf{c} \star (\mathbf{a}^H \mathbf{X}) = \mathbf{a}^H (\mathbf{c} \star \mathbf{X})$ . Target (main lobe) and interference (sidelobe) echoes are given by their delay and Doppler shift as  $s_k = c_{k-f_s \tau_1} \exp(j2\pi f_{D1} k / f_s)$  for an echo in the main lobe and  $r_k = c_{k-f_s \tau_2} \exp(j2\pi f_{D2} k / f_s)$  for an echo in the sidelobes. Modulating  $r_k$  by  $p_k$  and substituting in (10) gives

$$\chi_{\tau, f_D} = \sum_{k=k_0}^{k_0 + f_s CPI} c_{k-f_s \tau}^* \exp(-j2\pi f_D k / f_s) (s_k + p_k r_k + \eta_k), \quad (11)$$

which exhibits a peak where  $f_D = f_{D1}$  and  $\tau = \tau_1$ , but suppresses the result from  $r_k$  when the modulation rate of  $p_k$  is fast compared to the CPI. In matrix notation, (11) shows that  $\chi = \mathbf{c} \star \mathbf{y}_A$  represents the acquisition beam, and it can be shown that  $\chi = \mathbf{c} \star \mathbf{y}_S$  represents the SLS beam.

Efficient calculations subdivide (10) into intervals (PRIs), and use many PRIs to complete the CPI. Sequences of samples  $k$  are reshaped into matrices of fast time  $\tau$  and slow time  $T$ , where  $k = f_s(\tau + T)$ . Frequency-domain calculations are used to find the fast-time correlation for each PRI; these use the discrete Fourier transform (DFT)  $\mathbf{F}$ , implemented as the FFT,

$$\chi_T = \mathbf{F}^{-1} ((\mathbf{F} \mathbf{c}_T)^* \circ \mathbf{F} \mathbf{y}_T). \quad (12)$$

Next, a slow-time FFT is used to transform  $\chi_{\tau, T} \Rightarrow \chi_{\tau, f_D}$ .

If  $p_{\tau, T} = p_T$  is constant over each PRI, then  $\mathbf{y}_T$  in (12) is expanded into its constituent signals to describe the time-average acquisition CAF as

$$\chi_T^{(\bar{A})} = \mathbf{F}^{-1} ((\mathbf{F} \mathbf{c}_T)^* \circ \mathbf{F} (s_T + p_T r_T + \eta_T)). \quad (13)$$

This exhibits maxima at delays  $\tau$  corresponding to the echo time delays  $\tau_1$  and  $\tau_2$ . Considering only the columns corresponding to these maxima yields the responses

$$\chi_{\tau_1, T}^{(\bar{A})} \approx \exp(j2\pi f_{D1} T), \quad (14)$$

$$\chi_{\tau_2, T}^{(\bar{A})} \approx p_T \exp(j2\pi f_{D2} T). \quad (15)$$

The final FFT gives a peak at  $f_{D1}$  in (14), but  $p_T$  suppresses the response of (15). Since  $p_T$  is synchronous with the PRF, steps through (13) are identical for both the acquisition and SLS CAFs; (13) is decoded by multiplying by  $p_T$  as

$$\chi_T^{(\bar{S})} = p_T \chi_T^{(\bar{A})} = \mathbf{F}^{-1} ((\mathbf{F} \mathbf{c}_T)^* \circ \mathbf{F} (p_T s_T + r_T + p_T \eta_T)), \quad (16)$$

which yields the SLS CAF after the final FFT.

#### D. Architecture Anticipated for Add-On TMA-SLB

Analog and digital TMAs differ in the constraints on the weights  $a_{n,k}$  and in the methods of implementation. Whereas analog TMAs were developed for switches with  $a_{n,k} \in \{0, 1\}$ , the relaxed constraint  $a_{n,k} \in \mathbb{C}$  in digital systems can enable  $\hat{a}_{n,k} \in \mathbb{C}$  if an existing multiplier can be modulated with sufficient temporal accuracy. Reusing existing circuits enables implementing digital TMAs in existing digital beamformers,

with modifications only as-required to command modulating the weights  $\hat{a}_b$  selected among the beams  $b \in 1, 2, \dots, M$ .

A possible architecture anticipated for add-on TMA-SLB was shown in Fig. 1, and separates the control, beamformer, and detection subsystems. Although based on existing systems at the ATA, this is expected to be generalizable. High-level TMA-SLB control is shown as a software module similar to existing ones for generating antenna weights. This calculates  $\hat{a}_1$ ,  $\hat{a}_2$ , and the sequence  $p_k$ . These values are provided to the beamformer on register update cycles and the beamformer hardware is responsible for implementing the switching.

Switching between  $\hat{a}_1$  and  $\hat{a}_2$  within the beamformer hardware is a favored architecture because of both uncertain network latency and the comparatively slow cadence of software updates, given as 3 s by [65]. As shown in Fig. 1, the ATA beamformer lacks a dedicated module implementing  $a_{n,k}$ , but instead applies programmed coefficients  $|a_{n,k}|$  and  $\angle a_{n,k}$  separately. The first is applied by scaling the real-valued coefficients of a fractional delay filter  $b_{n,k}$ , and the second in a hardware fringe rotation circuit initialized with the angle  $\Theta_{n,k}$ . While each of these must be modulated to permit  $\hat{a}_{n,k} \in \mathbb{C}$ , the stricter constraint  $\hat{a}_{n,k} \in \mathbb{R}$ , used for the experiment in this paper, omits the need to modulate  $\Theta_{n,k}$ .

Finally, existing detectors are readily adapted to form the decoder and detector subsystem in Fig. 1. The synchronous decoder only requires changing the sign of the data in a manner aligned to the sequence  $p_k$ . Decoding a shared sequence can be synchronized using existing high-accuracy time-stamps embedded within data packets. Alternatively, selecting the rate of  $p_k$  as a subharmonic of the packet rate and encoding the state of  $p_k$  into the header of each packet eliminates the need for a priori sharing of the sequence. Since the SLS decoding and detection process is only needed for signals of ambiguous DOA, it might be invoked infrequently or limited to offline analysis of archived data.

## IV. OBSERVATIONS AT THE ALLEN TELESCOPE ARRAY

### A. Planning and Source Selection

An experiment was constructed to demonstrate and evaluate TMA-SLB using data collected at the ATA. Shown in Fig. 6, the ATA is described in detail by Welch [66] and consists of 42 six-meter parabolic dish antennas at the Hat Creek Radio Observatory (HCRO) in California. The sparse and aperiodic array presents a realistic setting and also challenges the optimization algorithms used to determine antenna weights. Spectrometry surveys at the ATA are a future application of TMA-SLB, and are sensitive to weak, transient signals detectable in 1 Hz bandwidths using long integrations.

For this experiment, the L-band hydroxyl maser W3(OH) was selected as a proxy target. Described by Wright [67], this maser is a strong, stable astronomical source that is well-characterized and detectable in short observations. The spectrum in Fig. 7, recorded with the ATA beamformer, shows the 1665 MHz and 1667 MHz spectral lines of the maser among a multitude of RFI. At least some of this RFI is self-generated and can be identified, including harmonics and subharmonics of the 838.8608 MHz

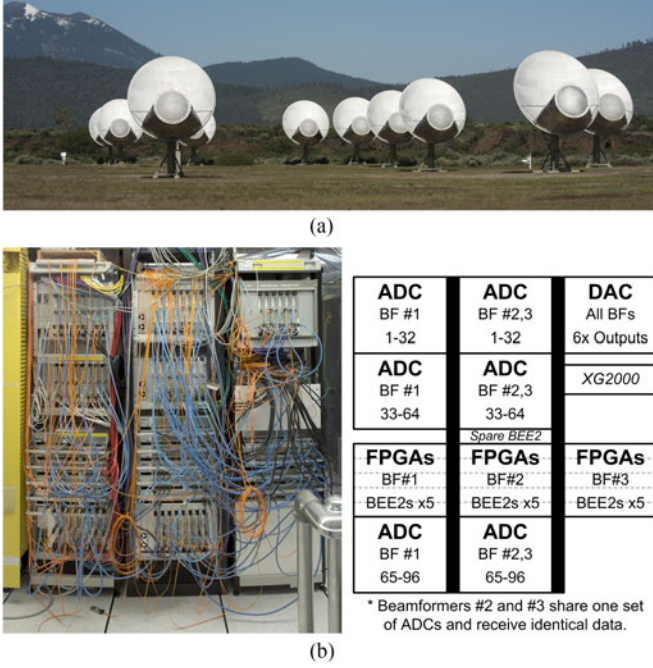


Fig. 6. The Allen Telescope Array and its beamformer subsystem. Reconfigurations described in Fig. 8 used FPGAs for BF 2 and 3. (a) Subset of the ATA's 42 antennas. (b) Photograph and layout of the beamforming & network equipment.

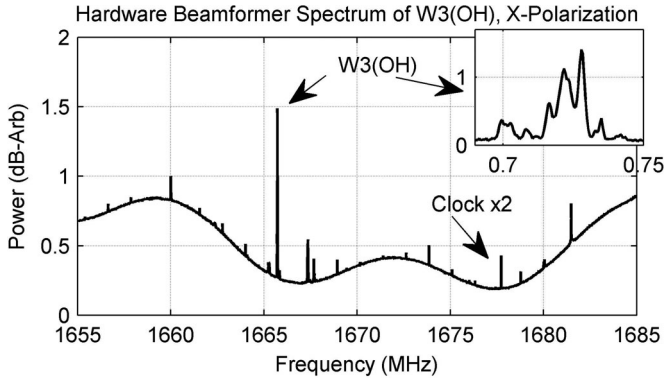


Fig. 7. Spectrum of W3(OH) among RFI, integrated for 200 s using the ATA beamformer and 6.4 kHz resolution. Inset shows a 512 Hz resolution spectrum of the maser line, relative to its 1665 MHz nominal frequency.

sample clock (illustrated at 1677.7216 MHz). The presence of significant RFI makes it difficult to identify the maser without a priori knowledge, and also presents a useful scenario for testing TMA-SLB.

Time series data for each available ATA antenna output (antpol) are obtained by engaging the ATA's Foxtrot direct-to-disk mode. Shown in Fig. 8, this mode reprograms the BEE2-based FPGAs of the real-time beamformer to become real-time packetizers. Input data at 104.8576 MCS/s are block-filtered by the packetizer using a 2048-point FFT. The output bandwidth is controlled by selecting which bins of the FFT are saved. The desired bins are encumbered with metadata including a hardware timestamp, sent to host computers via a 10 GbE network, and recorded to disk. Post processing inverts the FFT and creates synchronized time-domain data files of the antpols. The Foxtrot

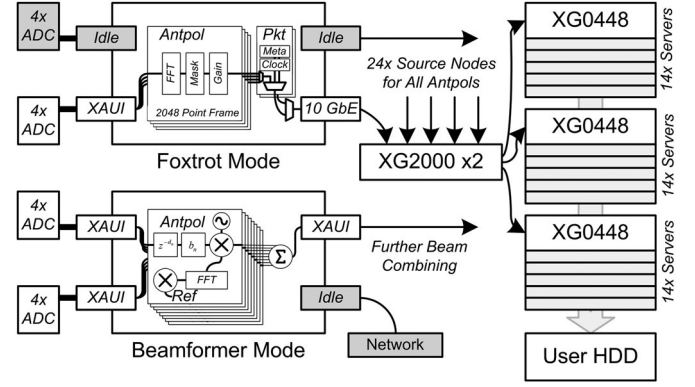


Fig. 8. Overview architecture of the Foxtrot system. A beamformer FPGA has one idle output connected to the 10 GbE network. The Foxtrot mode firmware engages this port. Packets from the FPGAs are distributed through a 10 GbE network (Fujitsu XG2000 and XG0448) for recording on servers.

TABLE I  
OBSERVATION SUMMARY DATA

Source	Purpose	Right Ascension and Declination	Azimuth and Elevation	Time <sup>a</sup> and Duration
CasA	Delay	23 h 23 m 26.8 s	1.9°, 71.9°	04:50:38
1362 Jy	Calibrator	+58° 48 m 28.0 s		2 min
3 c 48	Phase	1 h 37 m 41.3 s	95.3°, 62.6°	04:56:52
16.5 Jy	Calibrator	+33° 9 m 35.1 s		2 min
3 c 84	Phase	3 h 19 m 47.2 s	69.5°, 48.1°	05:05:11
23.9 Jy	Calibrator	+41° 30 m 42.1 s		5 min
W3(OH)	Target	2 h 27 m 3.9 s	35.5°, 57.5°	05:13:09
300 Jy		+61° 52 m 24.6 s		5 min

<sup>a</sup>All times are specified in UTC on 2013-10-30.

mode uses the BEE2s from two separate beamformers, since each packetizer model can accommodate half as many antpols as the beamformer model.

Observations occurred on 2013-10-30 from about 04:58 to 05:20 UTC. Foxtrot captured the band from 1663 MHz to 1675 MHz, which was selected to encompass the maser and RFI shown in Fig. 7. The resulting aggregate data rate of 10.5 Gbps included 55 recorded antpols, and rates varied from 197 to 777 Mbps to each host recorder. A total of 1.3 TB of data were recorded from the maser and three radio calibrators, as summarized in Table I. The first calibrator, Cassiopeia A (CasA), had a flux of 1362 Jy at the time of the observation [68], where  $1 \text{ Jy} = 10^{-26} \text{ W} \cdot \text{m}^{-2} \text{ Hz}^{-1}$ , and is used to calibrate the instrumental delay. The weaker phase calibrators 3C48 (16.5 Jy) and 3C84 (23.9 Jy) [69] are required because CasA does not stimulate the point source response of the ATA [70].

### B. Data Calibration and Steering

Recorded data represent uncorrected samples  $x_{n,k}$  from each antpol and must be calibrated and steered to produce the samples  $\hat{x}_{n,k}^{(\hat{A})}$  for beamforming. As shown in Fig. 1, steering adjusts the delay and phasor as  $\hat{x}_{n,k}^{(\hat{A})} = a_{n,k}^* (b_{n,k} * x_{n,k} * \delta_{d_{n,k}})$ , where  $a_{n,k}^* = \hat{a}_{n,k}^* a_{n,k}^{*(\text{BF})}$  comprises the TMA and beamformer correction phasors, and  $\delta_{d_{n,k}}$  and  $b_{n,k}$  implement full- and



fractional-sample delays. The phasor and delay corrections contain both geometric and instrumental components; while the former are deterministically calculated, the latter are estimated by cross-correlation of the calibrator data sets as  $\hat{\tau}_{2,1} = \mathbf{x}_2 \star \mathbf{x}_1$ , implemented as  $\mathbf{F}_{\hat{\tau}_{2,1}} = \sum (\mathbf{F}\mathbf{x}_2)^* \circ (\mathbf{F}\mathbf{x}_1)$ , which sums over successive data frames. The instrumental delay is estimated by finding  $\hat{\tau}_{2,1}$  satisfying  $\mathbf{F}_{\hat{\tau}_{2,1}}(\omega) \approx \exp(-j\omega\hat{\tau}_{2,1})$  over frequency  $\omega$ , using geometrically-corrected data from CasA. The instrumental phase  $\hat{\phi}_{2,1}$  between antennas is estimated from delay-calibrated 3C84 data, which is summed over frequency as  $\sum \mathbf{F}_{\hat{\tau}_{2,1}}(\omega) \approx \exp(j\omega\hat{\phi}_{2,1})$ . Calibration values are anchored to an arbitrary selection that  $\tau_1 = 0$  and  $\phi_1 = 0$ .

The magnitude  $|a_{n,k}^{*(\text{BF})}|$  reweights the antennas relative to the equal-RMS amplitudes ensured by the ADC's automatic gain control, e.g.,  $\text{var}(x_n) \approx \sigma^2 \forall n$ . Its value is selected based on the combining strategy, such as equal gain combining (EGC) [71] or maximal ratio combining (MRC) [72]. The former, EGC, sets each antenna to exhibit the same total noise power and yields the maximum sensitivity when the sensitivities of the individual antennas are unknown [71]. Although radio telescope sensitivities can be estimated by  $|\hat{\tau}_{2,1}|$ , [73] notes the diminished efficacy of MRC when considering typical calibration and beamforming errors. This work adopts  $|a_{n,k}^{*(\text{BF})}| = 1$  (EGC) to emulate the typical ATA observing mode.

### C. Solving for TMA-SLB Steering Weights

Beamformer outputs are created by summing calibrated values that have been steered toward the target of interest,  $\hat{x}_{n,k}$ , then adjusted by TMA phasors. Forming an EGC beam is compared to forming the acquisition and SLS beams as

$$\begin{aligned} y_k^{(\text{EGC})} &= \sum_{n=1}^N \hat{x}_{n,k}, \quad y_k^{(\bar{A})} = \sum_{n=1}^N \hat{a}_{n,k}^* \hat{x}_{n,k}, \\ y_k^{(\bar{S})} &= p_k \left( \sum_{n=1}^N \hat{a}_{n,k}^* \hat{x}_{n,k} \right). \end{aligned} \quad (17)$$

Coefficients are selected from the beams  $\hat{a}_{n,k} \in \hat{a}_{n,b}$  where  $b = \{1, 2\}$  according to a random zero-mean sequence  $\mathbf{p}$  so that  $\hat{a}_{n,k} = \hat{a}_{n,1}$  for  $p_k = -1$  and  $\hat{a}_{n,k} = \hat{a}_{n,2}$  when  $p_k = 1$ . The values of the coefficients  $\hat{a}_b$  can be synthesized with deterministic or optimization-based approaches [4], and optimization with a genetic algorithm (GA) is adopted here. GAs are well-known tools for array optimization [17], [21], although recent work describes alternative algorithms with improved convergence behavior (e.g., [74]).

The GA predicts radiation patterns  $F_b(\theta, \phi, \theta_L, \phi_L)$  (hereafter just  $F_b$ ) over look angles  $\theta_L, \phi_L$  resulting from an arrangement of antennas steered by  $\mathbf{a}^{(\text{BF})}$  to the steering direction  $\theta, \phi$  and weighted by  $\hat{\mathbf{a}}_b$  as

$$F_b(\theta, \phi, \theta_L, \phi_L) = \hat{\mathbf{a}}_b^H (\mathbf{a}^{*(\text{BF})}(\theta, \phi) \circ \mathbf{x}(\theta_L, \phi_L)). \quad (18)$$

Stimulus magnitudes in  $\mathbf{x}$  are simulated as equal since the antenna sensitivities are unknown. This assumption is an error source and topic for further study. The array factors  $F_b$  are analyzed using two figures of merit (FOMs). The first considers

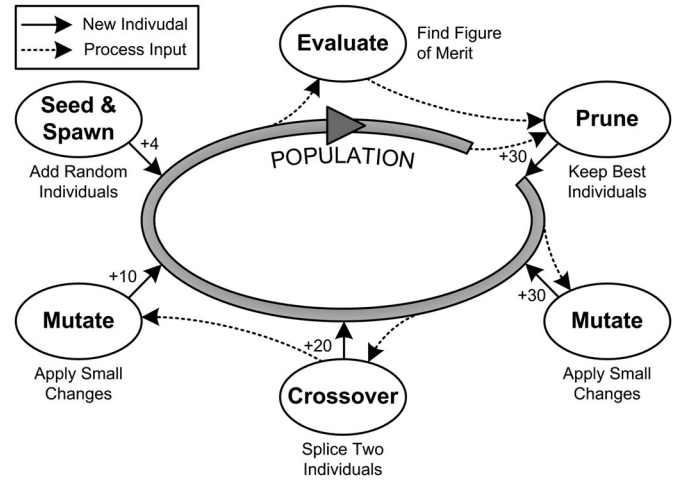


Fig. 9. Genetic algorithm used to optimize the beamformer weights. The GA begins by spawning 94 random individuals, and iterates for 500 generations. Numbers indicate the quantity of new individuals generated at each step.

the gain of acquisition beam main lobe  $ML$  as

$$FOM_G = \max_{\theta_L, \phi_L \in ML} \left( \frac{1}{4} |F_1 + F_2|^2 \right). \quad (19)$$

A second analysis considers the RMS level of the sidelobes, weighted by a characteristic called modulation normalized suppression, which describes the ratio between the sidelobes of the acquisition and SLS beams. Larger ratios enhance the effect of the modulation and are desirable. The relative importance of the sidelobes and modulation normalized suppression is controlled using a parameter  $C$  as

$$\begin{aligned} FOM_{SLL} &= \left( \frac{1}{N_\theta N_\phi} \sum_{\theta_L \notin ML} \sum_{\phi_L \notin ML} \left| \frac{F_1 + F_2}{2} \right|^{2C} \right. \\ &\quad \times \left. \left| \frac{F_1 + F_2}{F_1 - F_2} \right|^4 \right)^{-1/2}, \end{aligned} \quad (20)$$

where  $N_\theta$  and  $N_\phi$  represent the number of points in each summation. The two FOMs are weighted and combined into a final FOM, which is the GA's objective function, as

$$FOM = W_G 10 \log_{10} FOM_G + 10 \log_{10} FOM_{SLL}. \quad (21)$$

The present analyses used  $W_G = 1$  and  $C = 1$ ; while different choices will place differing emphases on the acquisition beam's main lobe gain ( $W_G$ ) and absolute sidelobe level ( $C$ ), the efficacy of other selections was not fully explored.

Fig. 9 shows the basic processes used by the GA in this work. This GA operates on a population of candidate weights (individuals), each of which is represented by a gene of length  $2N$ , formed as  $[|\hat{\mathbf{a}}_1|, |\hat{\mathbf{a}}_2|]$ . Entries are floating-point values constrained between  $[0, 10]$ . Restricting the GA to  $\hat{a}_{n,k} \in \mathbb{R}$  gave faster convergence than  $\hat{a}_{n,k} \in \mathbb{C}$  without degrading the results, although the broader case is implemented by including a second gene as  $[\angle \hat{\mathbf{a}}_1, \angle \hat{\mathbf{a}}_2]$ . The GA was initialized with 94 random individuals and retained the best 30 across each of 500 generations. Each generation comprises six major steps:

TABLE II  
PARTICIPATING X-POLARIZATION ANTENNAS, LOCATIONS, & WEIGHTS

Antenna and Name		North (m)	East (m)	Up (m)	$\hat{a}_{n,1}$	$\hat{a}_{n,2}$
1	1a	-177.323	-103.716	0.547	0.9412	0.9649
2	1b	-194.117	-69.515	0.319	0.8752	0.5560
3	1c	-257.973	-77.164	2.154	0.4611	0.8703
13	2c	-135.622	-58.933	0.401	0.8964	0.8577
14	2d	-156.99	-19.533	0.442	1.0034	0.6626
15	2e	-154.202	-2.215	0.428	1.3902	0.4231
16	2f	-140.48	-145.576	0.407	0.6057	0.2060
17	2g	-142.392	-174.643	0.487	0.6698	1.2227
19	2j	-115.098	-155.158	0.478	1.0632	0.7515
20	2k	-109.353	-145.571	0.529	0.8946	1.2372
23	3c	-65.119	-4.776	0.330	1.9314	0.1239
24	3d	-42.694	-51.075	0.291	1.3856	0.7649
25	3e	-53.696	-77.593	0.235	0.1506	1.4870
29	3j	-20.638	-45.62	0.263	0.0000	1.6849
30	3l	-0.793	-74.46	0.157	0.0002	1.7730
35	4j	26.229	-23.571	0.316	0.7125	1.1355
36	4k	0.245	-10.854	0.167	0.1507	1.3341
37	4l	0.013	-0.013	0.004	1.4158	0.6549
38	5b	-8.528	76.53	0.306	0.5427	1.3833
39	5c	-25.655	82.922	0.332	1.3139	0.6142

- 1) evaluate the population using (21) to determine the figure of merit for each individual,
- 2) prune the population to retain the 30 best individuals,
- 3) create 30 new individuals by mutation of randomly-selected individuals from the retained set,
- 4) create 20 new individuals by crossover of randomly-selected parents from the retained and mutated sets,
- 5) create 10 new individuals by mutation of randomly-selected individuals that were generated by crossover,
- 6) and finally, create 4 new individuals at random, to provide potentially-disruptive diversity.

Mutation was applied additively using random values from  $\mathcal{U}(-0.05\gamma, 0.05\gamma)$ ;  $\gamma$  decays exponentially from 1 to  $e^{-5}$  over the 500 generations to improve convergence. Crossover was applied by concatenating genes from two parents using a randomly-selected crossover point; values preceding this point are copied from the first parent, and values after this point are copied from the second parent. Selections of individuals for mutation and crossover are made at random with replacement.

Analyses for the present experiment optimized patterns for a subset of 20 usable X-polarization ATA antpols steered to the direction of W3(OH). The GA was executed 100 times to obtain a distribution of results. These antennas, their locations, and the final optimized weights  $\hat{a}_{n,b}$  are given in Table II. The large size of the ATA, and arcmin-scale pattern features, make evaluating the full radiation pattern untenable in the GA. Instead, the GA considered one slice in elevation, evaluated in  $30''$  intervals within  $\pm 1^\circ$  of the pointing direction. This extent is similar to the 3 dB beamwidth of the ATA's antennas.

The radiation patterns of the best result from the GA are plotted in Figs. 10 and 11. First, Fig. 10 shows the optimized 1D pattern slices of the predicted acquisition and SLS beams. This figure illustrates the challenge of optimizing a large sparse array. While [4] showed that half-wavelength-spaced linear TMAs

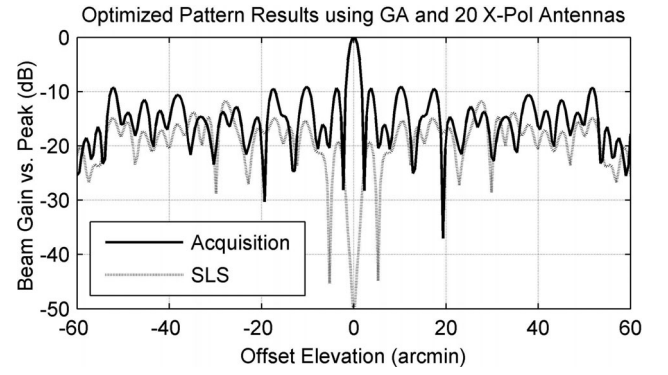


Fig. 10. Normalized acquisition and SLS patterns as optimized by the GA for the X-Pol beam directed toward the target W3(OH). Pointing losses due to the TMA are estimated at 1.1 dB.

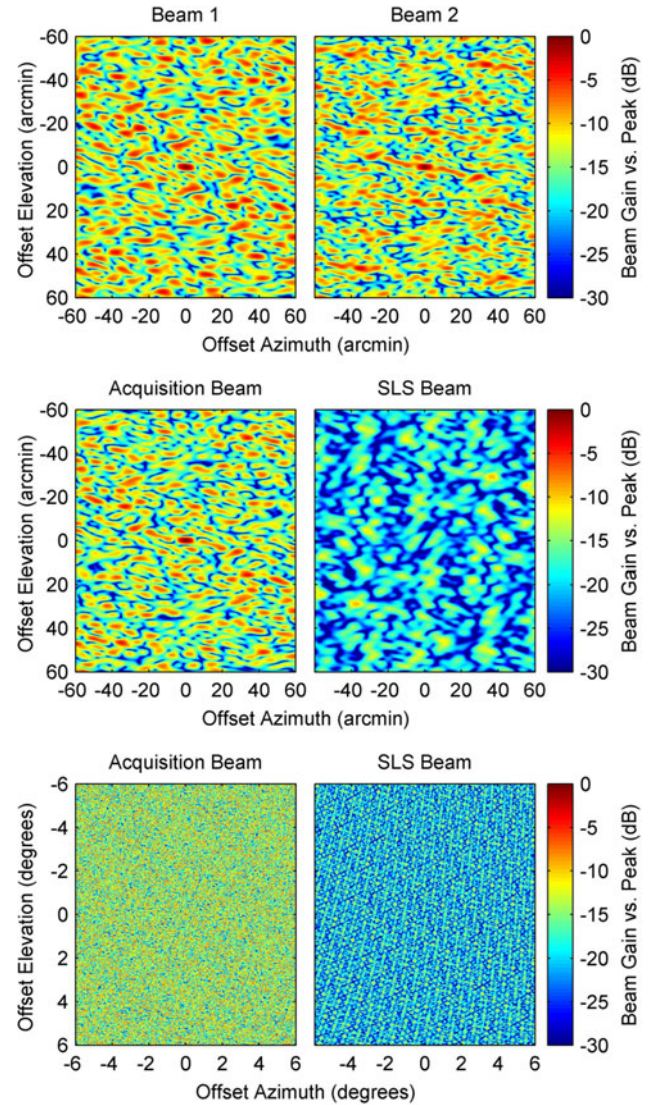


Fig. 11. Two-dimensional structure of the optimized beams, simulated near the target's direction. At top, patterns of the two physical beams used in switching. At middle and bottom, patterns of the multiplexed subbeams within  $1^\circ$  and  $6^\circ$  of the target. The subbeam responses are similar to Fig. 10, which represented a vertical slice through these plots at an azimuth offset of  $0^\circ$ .



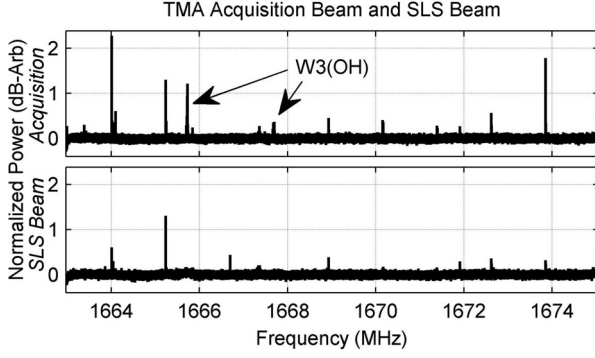


Fig. 12. Integrated acquisition and SLS beams. Modulation rate is 240 kHz and spectral resolution is 51.2 Hz.

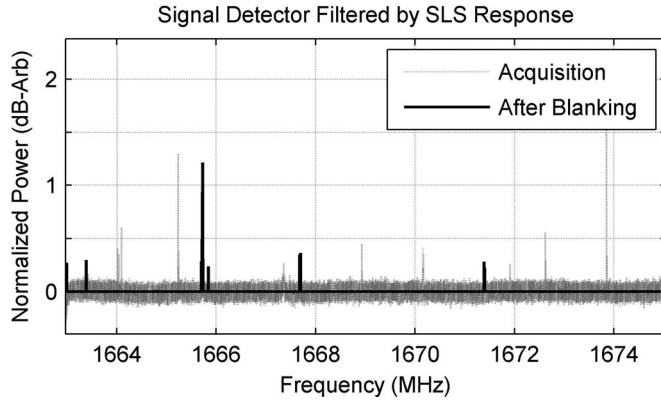


Fig. 13. Acquisition beam data (light gray) overlaid with results of the signal detector implementing exclusion by the SLS beam.

easily exhibit  $F_{\bar{S}} > F_{\bar{A}}$  throughout the sidelobes, a criterion desirable for implementing Maisel SLB, this subset of ATA antennas provided insufficient degrees of freedom for the algorithm to achieve that criterion throughout the beam. Analysis of the 2D pattern in Fig. 11 shows that this criterion is maintained in only about 30% of angles and that the median difference between the acquisition and SLS patterns is about 3 dB. Failing to maintain  $F_{\bar{S}} > F_{\bar{A}}$  throughout the sidelobes enables weak RFI to trigger false alarms, as described by [2]. The bottom panel of Fig. 11 shows that these characteristics are retained outside the  $\pm 1^\circ$  optimization region and beyond the main lobe of the ATA's antennas. Differences among the responses of the individual antennas make it difficult to predict meaningful patterns for the farther sidelobes.

#### D. Blanking Analysis and Results

The optimized TMA coefficients in Table II were applied to the calibrated, steered data for W3(OH) according to (17) to create the acquisition and SLS beams. The sequence  $\mathbf{p}$  was formed from a uniformly distributed random variable  $\text{sgn}(\mathcal{U}(-1, 1))$ . The modulation rate of  $\mathbf{p}$  is 240 kHz and was selected so that the modulation adequately suppressed the maser signals below the noise floor. Spectra of the resulting acquisition beam  $\mathbf{y}_{\bar{A}}$  and SLS beam  $\mathbf{y}_{\bar{S}}$  are illustrated in Fig. 12. These spectra are normalized by the baseline noise power response, use a resolution of 51.2 Hz to enhance the RFI, and are integrated for 300 s.

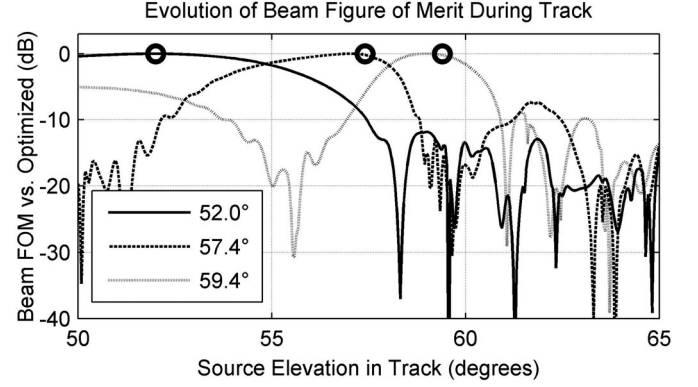


Fig. 14. Evolution of the computed figure of merit when a solution optimized for a specific pointing direction is used at other pointing directions, showing the need to update the TMA weights as the array pointing direction changes. The first and second points are about 47 minutes apart. The second and third points are about 18 minutes apart. Plotted using ephemeris for W3(OH).

Both beams contain a multitude of observable signals, but initial inspection reveals that the target maser is observed only in the acquisition beam, just below 1666 and 1668 MHz.

The spectra in Fig. 12 were processed with a simple threshold-based SLB algorithm. A detector  $D(\cdot)$  identified signals more than  $5\sigma$  above the noise floor variation (in dB), and candidate signals satisfying  $D(\mathbf{y}_{\bar{A}}) > 5\sigma$  were filtered to exclude any signals where  $D(\mathbf{y}_{\bar{S}}) > 5\sigma$ . Results of the blanking are shown in Fig. 13, in which the spectrum of the acquisition beam (lighter) is overlaid with the spectrum after blanking (darker). Blanking excluded nine distinct RFI signals leaving only the two maser lines and four weak RFI signals.

#### V. CONCLUSION

These results represent the first experiments applying TMA-SLB to a physical array, and show the promise of this technique in a realistic setting. By utilizing beamformer time modulation with a relaxed goal of identifying (not nulling) RFI, nine-of-thirteen RFI signals in Fig. 13 were successfully excluded without increasing the beamformer's computational complexity. Both the sparse spectrum (enabling the relaxed goal) and constrained computational assets (limiting the complexity of the approach) are stipulations of the problems for which TMA-SLB was created.

Absent computational restrictions, TMA-SLB's approach of open-loop discrimination offers complementary advantages to the capabilities of other techniques (e.g., sidelobe cancellers and adaptive nulls), which support its use against weak RFI in hybrid approaches. First, TMA-SLB operates on the timescale of the detector, rather than the shorter timescale required for adaptivity; this improves sensitivity to weak RFI, and can also mitigate potential confusion between signals that correlate on the shorter timescales. Second, SLB can require fewer degrees of freedom than pattern nulls when used against a multitude of spatially-diverse RFI; this enables inexpensively blanking the ubiquity of weak RFI while reserving nulls or sidelobe cancellers for the strongest interferers.

In addition to showing the promise of TMA-SLB, this work identified several challenges in applying TMA synthesis to large aperiodic arrays, which suggest areas of future work. First, algorithms for coefficient synthesis should be improved so that they will be useable in a deployed system. Although the GA is a useful analysis tool, the uncertain convergence and long computation time make it unsuited to real-time operation, especially since the optimal solution depends on the steering angle. As illustrated in Fig. 14, the FOM calculated using (21) degrades when solutions are used at steering angles other than that for which they were optimized.

A second area of future work is determining whether the optimization results found for the ATA subarray represent a poor optimization or a limit on the sidelobe level of the patterns of the sparse array. In the latter case, multibeam approaches should be investigated to synthesize a plurality of SLS beams, with different sidelobe structures, to cooperatively attain the desirable quality of  $F_S > F_A$  in the sidelobes. If attainable, meeting this criterion would improve the ability of TMA-SLB to exclude weak sidelobe interference.

Finally, the effect of pattern errors should be explored, particularly with regard to the anticipated efficacy of TMA-SLB. Section IV-C identified the assumption of equal signal levels and the use of EGC as one source of error. Additionally, near-field sources can enter antennas with significantly different power levels, and Harp [75] reported differences in the far sidelobes of the ATA's primary antennas that can affect far-field RFI. Finally, [73] noted passband amplitude and phase variations in the ATA that are not correctable by the hardware beamformer. Studying each of these will provide an improved understanding of the expected behavior of a deployed implementation of TMA-SLB used to identify and reject spectrally-separable narrow-band RFI.

#### ACKNOWLEDGMENT

The authors are grateful to the staff of the SETI Institute and the Allen Telescope Array for their support throughout this experiment. In particular, Mr. Jon Richards of the SETI Institute is thanked for his invaluable on-site assistance.

#### REFERENCES

- [1] L. Maisel, "Performance of sidelobe blanking systems," *IEEE Trans. Aerosp. Electron. Syst.*, vol. AES-4, no. 2, pp. 174–180, Mar. 1968.
- [2] O. Coskun and C. Candan, "On the optimality of Maisel sidelobe blanking structure," in *Proc. 2014 IEEE Radar Conf.*, Cincinnati, OH, USA, pp. 1102–1107.
- [3] D. A. Shnidman and N. R. Shnidman, "Sidelobe blanking with expanded models," *IEEE Trans. Aerosp. Electron. Syst.*, vol. 47, no. 2, pp. 790–805, Apr. 2011.
- [4] W. C. Barott and B. Himed, "Time-modulated array pattern for sidelobe blanking in spectrometry and radar," *IEEE Antennas Wireless Propag. Lett.*, vol. 13, pp. 1015–1018, 2014.
- [5] W. C. Barott and S. Fucharoen, "Applying beamformer time modulation to blank sidelobes," presented at the 2014 IEEE Benjamin Franklin Symp. on Microwave Antenna Subsystem Radar, Telecommun., Biomedical Applications, Philadelphia, PA, USA, Sep. 27, 2014.
- [6] A. Appelbaum and L. Kaplan, "Sidelobe suppression considerations in the design of an electronically steered IFF antenna," *IEEE Trans. Antennas Propag.*, vol. AP-24, no. 4, pp. 425–432, Jul. 1976.
- [7] Collision of Aeronaves De Mexico, S.A. McDonnell Douglas DC-9–32, XA-JED and Piper PA-28–181, N4891F, National Transportation Safety Board, Washington, DC, USA, Aircraft Accident Rep. no. AAR-87/07, 1987.
- [8] Report: US Army UH60 Black Hawk Helicopters 87–26000 and 88–26060, Volume 7, Tabs O-4 thru Q, Page 13 (file page 173), Aircraft Accident Investigation Board, Washington, DC, USA, Tech. Rep. UH-60 Black Hawk Identification Friend or Foe (IFF System). [Online]. Available: [http://www.dod.mil/pubs/foi/Reading\\_Room/Other/973-7.pdf](http://www.dod.mil/pubs/foi/Reading_Room/Other/973-7.pdf)
- [9] D. R. Lorimer, M. Bailes, M. A. McLaughlin, D. J. Narkevic, and F. Crawford, "A bright millisecond radio burst of extragalactic origin," *Science*, vol. 318, no. 5851, pp. 777–780, Nov. 2007.
- [10] D. Thornton *et al.*, "A population of fast radio bursts at cosmological distances," *Science*, vol. 341, no. 6141, pp. 53–56, Jul. 2013.
- [11] S. Burke-Spolaor, M. Bailes, R. Ekers, J.-P. Macquart, and F. Crawford III, "Radio bursts with extragalactic spectral characteristics show terrestrial origins," *Astrophys. J.*, vol. 727, no. 1, Jan. 2011, Art. no. 18.
- [12] R. H. Gray and K. B. Marvel, "A VLA search for the Ohio State 'Wow,'" *Astrophys. J.*, vol. 546, no. 2, pp. 1171–1177, Jan. 2001.
- [13] R. H. Gray and S. Ellingsen, "A search for periodic emissions at the Wow locale," *Astrophys. J.*, vol. 578, no. 2, pp. 967–971, Oct. 2002.
- [14] Setiquest, "Activity 26, 2012," 2012. [Online]. Available: <http://setiquest.info/mlfiles2/indexes/2012-08-09/index.html>
- [15] C. L. Dolph, "A current distribution for broadside arrays which optimizes the relationship between beam width and side-lobe level," *Proc. IRE*, vol. 34, no. 6, pp. 335–348, Jun. 1946.
- [16] W. Kummer, A. Villeneuve, T. Fong, and F. Terrio, "Ultra-low sidelobes from time-modulated arrays," *IEEE Trans. Antennas Propag.*, vol. AP-11, no. 6, pp. 633–639, Nov. 1963.
- [17] R. L. Haupt, "Thinned arrays using genetic algorithms," *IEEE Trans. Antennas Propag.*, vol. 42, no. 7, pp. 993–999, Jul. 1994.
- [18] R. Willey, "Space tapering of linear and planar arrays," *IRE Trans. Antennas Propag.*, vol. AP-10, no. 4, pp. 369–377, Jul. 1962.
- [19] R. Harrington, "Sidelobe reduction by nonuniform element spacing," *IRE Trans. Antennas Propag.*, vol. 9, no. 6, pp. 187–192, Mar. 1961.
- [20] A. Ishimaru, "Unequally spaced arrays based on the Poisson sum formula," *IEEE Trans. Antennas Propag.*, vol. 62, no. 4, pp. 1549–1554, Apr. 2014.
- [21] M. G. Bray, D. H. Werner, D. W. Boeringer, and D. W. Machuga, "Optimization of thinned aperiodic linear phased arrays using genetic algorithms to reduce grating lobes during scanning," *IEEE Trans. Antennas Propag.*, vol. 50, no. 12, pp. 1732–1742, Dec. 2002.
- [22] D. C.-J. Bock, "The antenna configuration of the allen telescope array," Radio Astron. Lab., Univ. California Berkeley, Berkeley, CA, USA, ATA Memo Series 50, Jan. 8, 2003.
- [23] H. Subbaram and K. Abend, "Interference suppression via orthogonal projections: A performance analysis," *IEEE Trans. Antennas Propag.*, vol. 41, no. 9, pp. 1187–1194, Sep. 1993.
- [24] C. Fröh and T. Schildknecht, "Accuracy of two-line-element data for geostationary and high-eccentricity orbits," *J. Guidance, Control, Dyn.*, vol. 35, no. 5, pp. 1483–1491, Sep. 2012.
- [25] T. S. Kelso, "Validation of SGP4 and IS-GPS-200D against GPS precision ephemerides," in *Proc. 17th AAS/AIAA Space Flight Mech. Meeting*, Sedona, AZ, USA, 2007, AAS07–127, pp. 1–14.
- [26] B. Widrow, P. E. Mantey, L. J. Griffiths, and B. B. Goode, "Adaptive antenna systems," *Proc. IEEE*, vol. 55, no. 12, pp. 2143–2159, Dec. 1967.
- [27] L. E. Brennan and I. S. Reed, "Theory of adaptive radar," *IEEE Trans. Aerosp. Electron. Syst.*, vol. AES-9, no. 2, pp. 237–252, Mar. 1973.
- [28] A. Farina, "Single sidelobe canceller: Theory and evaluation," *IEEE Trans. Aerosp. Electron. Syst.*, vol. AES-13, no. 6, pp. 690–699, Nov. 1977.
- [29] J. E. Palmer and S. J. Searle, "Evaluation of adaptive filter algorithms for clutter cancellation in passive bistatic radar," in *Proc. 2012 IEEE Radar Conf.*, Atlanta, GA, USA, pp. 493–498.
- [30] F. Colone, D. W. O'Hagan, P. Lombardo, and C. J. Baker, "A multistage processing algorithm for disturbance removal and target detection in passive bistatic radar," *IEEE Trans. Aerosp. Electron. Syst.*, vol. 45, no. 2, pp. 698–722, Apr. 2009.
- [31] R. Perley, "Attenuation of radio frequency interference by interferometric fringe rotation," EVLA Memo Series 49, Nov. 2002.
- [32] J. A. Högbom, "Aperture synthesis with a non-regular distribution of interferometer baselines," *Astron. Astrophys. Suppl.*, vol. 15, pp. 417–426, Jun. 1974.
- [33] K. Kulpa, "The CLEAN type algorithms for radar signal processing," in *Proc. 2008 Microw., Radar Remote Sens. Symp.*, Kiev, Ukraine, pp. 152–157.

- [34] W. C. Barott, "Volumetric phased arrays for satellite communications," Ph.D. dissertation, Dept. Elect. Comput. Eng., Georgia Inst. Technol., Atlanta, GA, USA, 2006.
- [35] M. Daun, U. Nickel, and W. Koch, "Tracking in multistatic passive radar systems using DAB/DVB-T illumination," *Signal Process.*, vol. 92, no. 6, pp. 1365–1386, Jun. 2012.
- [36] H. E. Shanks and R. W. Bickmore, "Four-dimensional electromagnetic radiators," *Can. J. Physics*, vol. 37, no. 3, pp. 263–275, Mar. 1959.
- [37] B. Hatcher, "General time-modulated antenna arrays," in *Proc. 1966 Antennas Propag. Soc. Int. Symp.*, pp. 75–78.
- [38] P. G. Hansel, "Navigation system," *U.S. Patent 2 490 050*, Dec. 6, 1949.
- [39] P. G. Hansel, "Doppler-effect omnirange," *Proc. IRE*, vol. 41, no. 12, pp. 1750–1756, Dec. 1953.
- [40] Federal Radionavigation Plan, Department of Defense, Department of Homeland Security, and Department of Transportation, 2012.
- [41] F. R. Dickey, M. Labitt, and F. M. Staudaher, "Development of airborne moving target radar for long range surveillance," *IEEE Trans. Aerosp. Electron. Syst.*, vol. 27, no. 6, pp. 959–972, Nov. 1991.
- [42] B. Dawidowicz, K. S. Kulpa, M. Malanowski, J. Misiurewicz, P. Samczynski, and M. Smolarczyk, "DPCA detection of moving targets in airborne passive radar," *IEEE Trans. Aerosp. Electron. Syst.*, vol. 48, no. 2, pp. 1347–1357, Apr. 2012.
- [43] G. Li, S. Yang, and Z. Nie, "Direction of arrival estimation in time modulated linear arrays with unidirectional phase center motion," *IEEE Trans. Antennas Propag.*, vol. 58, no. 4, pp. 1105–1111, Apr. 2010.
- [44] Y. Tong and A. Tennant, "A two-channel time modulated linear array with adaptive beamforming," *IEEE Trans. Antennas Propag.*, vol. 60, no. 1, pp. 141–147, Jan. 2012.
- [45] B. Lewis and J. E. Evans, "A new technique for reducing radar response to signals entering antenna sidelobes," *IEEE Trans. Antennas Propag.*, vol. AP-31, no. 6, pp. 993–996, Nov. 1983.
- [46] R. L. Haupt, "Time-modulated receive arrays," in *Proc. 2011 IEEE Int. Symp. Antennas Propag.*, Spokane, WA, USA, pp. 968–971.
- [47] S. Yang, Y. B. Gan, and A. Qing, "Low sidelobe phased array antennas with time modulation," in *Proc. 2003 IEEE Antennas Propag. Soc. Int. Symp.*, Columbus, OH, USA, pp. 200–203.
- [48] J. Fondevila, J. C. Bregains, F. Ares, and E. Moreno, "Optimizing uniformly excited linear arrays through time modulation," *IEEE Antennas Wireless Propag. Lett.*, vol. 3, no. 1, pp. 298–301, Dec. 2004.
- [49] L. Poli, P. Rocca, L. Manica, and A. Massa, "Handling sideband radiations in time-modulated arrays through particle swarm optimization," *IEEE Trans. Antennas Propag.*, vol. 58, no. 4, pp. 1408–1411, Apr. 2010.
- [50] Y. Tong and A. Tennant, "Beam steering and adaptive nulling of low sidelobe level time-modulated linear array," in *Proc. 5th Eur. Conf. Antennas Propag.*, Rome, Italy, 2011, pp. 948–951.
- [51] Y. Chen, S. Yang, Gang Li, and Z. Nie, "Adaptive nulling in time-modulated antenna arrays," in *Proc. 8th Int. Symp. Antennas, Propag., EM Theory*, Kunming, China, 2008, pp. 713–716.
- [52] L. Poli, P. Rocca, G. Oliveri, and A. Massa, "Adaptive nulling in time-modulated linear arrays with minimum power losses," *IET Microw., Antennas Propag.*, vol. 5, no. 2, pp. 157–166, Jan. 2011.
- [53] P. Rocca, L. Poli, G. Oliveri, and A. Massa, "Adaptive nulling in time-varying scenarios through time-modulated linear arrays," *IEEE Antennas Wireless Propag. Lett.*, vol. 11, pp. 101–104, 2012.
- [54] G. Li, S. Yang, Y. Chen, and Z.-P. Nie, "A novel electronic beam steering technique in time modulated antenna array," *Prog. Electromagn. Res.*, vol. 97, pp. 391–405, 2009.
- [55] L. Poli, P. Rocca, G. Oliveri, and A. Massa, "Harmonic beamforming in time-modulated linear arrays," *IEEE Trans. Antennas Propag.*, vol. 59, no. 7, pp. 2538–2545, Jul. 2011.
- [56] A. Tennant and B. Chambers, "A two-element time-modulated array with direction-finding properties," *IEEE Antennas Wireless Propag. Lett.*, vol. 6, pp. 64–65, 2007.
- [57] P. Rocca, Q. Zhu, E. T. Bekele, S. Yang, and A. Massa, "4-D Arrays as enabling technology for cognitive radio systems," *IEEE Trans. Antennas Propag.*, vol. 62, no. 3, pp. 1102–1116, Mar. 2014.
- [58] M. P. Daly, E. L. Daly, and J. T. Bernhard, "Demonstration of directional modulation using a phased array," *IEEE Trans. Antennas Propag.*, vol. 58, no. 5, pp. 1545–1550, May 2010.
- [59] W. C. Barott, "Nonsinusoidal TMA basis functions and the DVOR," in *Proc. 2015 IEEE Int. Symp. Antennas Propag.*, Vancouver, BC, Canada, pp. 810–811.
- [60] G. Li, S. Yang, and Z. Nie, "A Study on the application of time modulated antenna arrays to airborne pulsed Doppler radar," *IEEE Trans. Antennas Propag.*, vol. 57, no. 5, pp. 1579–1583, May 2009.
- [61] J. Euzière, R. Guinvarc'h, B. Uguen, and R. Gillard, "Optimization of sparse time-modulated array by genetic algorithm for radar applications," *IEEE Antennas Wireless Propag. Lett.*, vol. 13, pp. 161–164, 2014.
- [62] J. Euzière, R. Guinvarc'h, M. Lesturgie, B. Uguen and R. Gillard, "Dual function radar communication time-modulated array," in *Proc. 2014 IEEE Int. Radar Conf.*, Lille, France, pp. 1–4.
- [63] M. Malanowski and K. Kulpa, "Digital beamforming for passive coherent location radar," in *Proc. 2008 IEEE Radar Conf.*, Rome, Italy, pp. 1–6.
- [64] H. Sun, D. K. P. Tan, and Y. Lu, "Aircraft target measurements using a GSM-based passive radar," in *Proc. 2008 IEEE Radar Conf.*, Rome, Italy, pp. 1–6.
- [65] W. C. Barott *et al.*, "Real-time beamforming using high-speed FPGAs at the Allen Telescope Array," *Radio Sci.*, vol. 46, Feb. 2011, Art. no. RS1016.
- [66] J. Welch *et al.*, "The Allen Telescope Array: The first widefield, panchromatic, snapshot radio camera for radio astronomy and SETI," *Proc. IEEE*, vol. 97, no. 8, pp. 1438–1447, Aug. 2009.
- [67] M. Wright, "Probing the star-forming region W3(OH) with ground-state hydroxyl masers," Ph.D. dissertation, Dept. Chem., Univ. Bristol, Bristol, U.K., 2001.
- [68] J. W. M. Baars, R. Genzel, I. I. K. Pauliny-Toth, and A. Witzel, "The absolute spectrum of CAS A – an accurate flux density scale and a set of secondary calibrators," *Astron. Astrophys.*, vol. 61, no. 1, pp. 99–106, Oct. 1977.
- [69] National Radio Astronomy Observatory, "The VLA calibrator manual." [Online]. Available: <http://www.vla.nrao.edu/astro/calib/manual/csource.html>
- [70] R. G. Conway, "The angular diameter of the radio-stars Cygnus A and Cassiopeia A," *Observatory*, vol. 76, pp. 235–237, Dec. 1956.
- [71] B. Barrow, "Diversity combination of fading signals with unequal mean strengths," *IEEE Trans. Commun. Syst.*, vol. CS-11, no. 1, pp. 73–78, Mar. 1963.
- [72] D. G. Brennan, "Linear diversity combining techniques," *Proc. IRE*, vol. 47, no. 6, pp. 1075–1102, Jun. 1959.
- [73] W. C. Barott, "Effect of beamforming errors on the efficacy of maximal ratio and equal gain combining," in *Proc. 2014 IEEE SoutheastCon*, Lexington, KY, USA, pp. 1–4.
- [74] M. Benedetti, R. Azaro, and A. Massa, "Memory enhanced PSO-based optimization approach for smart antennas control in complex interference scenarios," *IEEE Trans. Antennas Propag.*, vol. 56, no. 7, pp. 1939–1947, Jul. 2008.
- [75] G. R. Harp *et al.*, "Primary beam and dish surface characterization at the Allen Telescope Array by radio holography," *IEEE Trans. Antennas Propag.*, vol. 59, no. 6, pp. 2004–2021, Jun. 2011.



**William C. Barott** (M'06–SM'14) received the B.S., M.S., and Ph.D. degree from the Georgia Institute of Technology, Atlanta, GA, USA. In 2006, he joined Embry-Riddle Aeronautical University, Daytona Beach, FL, USA, and is currently a Professor in the Department of Electrical, Computer, Software, and Systems Engineering. His research interests include antenna arrays, modeling & simulation for passive radar, and radio astronomy.

He is a member of the American Institute of Aeronautics and Astronautics, and of the American Society for Engineering Education.



**Sugoon Fucharoen** received the B.S. in electrical engineering from Stanford University, Stanford, CA, USA, in 2012, and the M.S. in electrical and computer engineering from Embry-Riddle Aeronautical University, Daytona Beach, FL, USA in 2014. He is currently employed by Aeronautical Radio of Thailand, working on implementing cross-border Air Traffic Flow Management framework for the Asia-Pacific region.